

MASARYKOVA UNIVERZITA
Přírodovědecká fakulta
Ústav teoretické fyziky a astrofyziky



BAKALÁŘSKÁ PRÁCE
**Rentgenová studie detailů struktur v jetu NGC
4486**

Eva Kosová

Vedoucí bakalářské práce: Mgr. Filip Hroch, Ph.D.

2021

Bibliografický záznam

Autor:	Eva Kosová Přírodovědecká fakulta, Masarykova univerzita Ústav teoretické fyziky a astrofyziky
Název práce:	Rentgenová studie detailů struktur v jetu NGC 4486
Studijní program:	Fyzika
Studijní obor:	Astrofyzika
Vedoucí práce:	Mgr. Filip Hroch, Ph.D
Akademický rok:	2020/2021
Počet stran:	vii + 40
Klíčová slova:	Jet; Rentgen; Vlastní pohyb; Změny jasnosti, CIAO software; Rentgenová observatoř Chandra

Bibliographic Entry

Author: Eva Kosová
Faculty of Science, Masaryk University
Department of physics and astrophysics

Title of Thesis: A X-ray study on fine structures in a jet of NGC 4486

Degree Programme: Physics

Field of Study: Astrophysics

Supervisor: Mgr. Filip Hroch, Ph.D

Academic Year: 2020/2021

Number of Pages: vii + 40

Keywords: Jet; X-ray; Proper motion; Changes in brightness; CIAO software; Chandra X-ray observatory

Abstrakt:

Jet v centrální galaxii NGC 4486 v Kupě galaxií v Panně objevil čirou náhodou Curtis na fotografických deskách před více než sto lety jako „a curious straight ray . . . connected with the nukleus“.

Postupem času se u radioastronomických technik významně zlepšilo úhlové rozlišení obrazů vzdálených galaxií, což umožnilo studovat velmi jemné detaily galaktický jetů. Tato pozorování odhalila neočekávanou vlastnost, a to superluminiální pohyb. V poslední době je možné pozorovat v rentgenovém oboru jak úhlovou, tak i časovou variabilitu některých detailních struktur jetu. Studium v rentgenovém oboru je velmi atraktivní a to zejména proto, že nám pomáhá vykreslovat obraz dosud nespatřených fyzikálních procesů.

Cílem této práce je studie dvou již zmíněných metod a také samotné struktury jetu NGC 4486. Nejnovější pokročilé metody, veškerá analýza dat, zpracování obrazu, matematické statistiky a zpracování kosmických pozorování, jakožto i hluboké astrofyzikální zázemí, je nezbytné pro výsledky práce.

Abstract:

The jet of the nucleus of NGC 4486, central galaxy in Virgo cluster, has been incidentally discovered by Curtis on photographic plates over one hundredth years ago as "a curious straight ray . . . connected with the nucleus".

Over time, resourceful radio-astronomical techniques have significantly improved angular resolution of distant galaxies images, allowing to study of very fine details in the jets. These observations revealed an unexpected property of the jet – the superluminal motion. Recently, it is possible to observe, in X-rays, of both angular and time variability of some structure details in the jet. The study in X-rays is very attractive; one paints a picture of background physical processes, unseen yet.

The working goal of this thesis is to study both of the methods, and the fine structure itself, of the jet of NGC 4486. Recent advanced methods of all data analysis, image processing, mathematical statistics, and processing of spacecraft observations, as well as a deep astrophysical background are necessary for valuable results.

ZADÁNÍ
BAKALÁŘSKÉ PRÁCE

Akademický rok: 2020/2021

Ústav:	Ústav teoretické fyziky a astrofyziky
Studentka:	Eva Kosová
Program:	Fyzika
Obor:	Astrofyzika

Ředitel *ústavu* PŘF MU Vám ve smyslu Studijního a zkušebního řádu MU určuje bakalářskou práci s názvem:

Název práce:	Rentgenová studie detailů struktur v jetu NGC 4486
Název práce anglicky:	A X-ray study on fine structures in a jet of NGC 4486
Jazyk závěrečné práce:	angličtina

Oficiální zadání:

The jet of the nucleus of NGC 4486, central galaxy in Virgo cluster, has been incidentally discovered by Curtis on photographic plates over one hundredth years ago as "a curious straight ray ... connected with the nucleus".

Over time, resourceful radio-astronomical techniques has significantly improved angular resolution of distant galaxies images, allowing to study of very fine details in the jets. These observation revealed an unexpected property of the jet – the superluminal motion.

Recently, it is possible to observe, in X-rays, of both angular and time variability of some structure details in the jet. The study in X-rays is very attractive; one paints a picture of background physical processes, unseen yet.

The working goal of this thesis is to study of both the methods, and the fine structure itself, of the jet of NGC 4486. Recent advanced methods of all data analysis, image processing, mathematical statistics and a processing of spacecraft observations, as well as a deep astro-physical background are necessary for valuable results.

Vedoucí práce:	Mgr. Filip Hroch, Ph.D.
Konzultant:	Mgr. Jean-Paul Bernhard Riffald Souza Breuer
Datum zadání práce:	24. 11. 2020
V Brně dne:	13. 6. 2021

Zadání bylo schváleno prostřednictvím IS MU.

Eva Kosová, 21. 1. 2021

Mgr. Filip Hroch, Ph.D., 26. 1. 2021

Mgr. Michael Krbek, Ph.D., 1. 2. 2021

Touto cestou bych ráda poděkovala panu Filipu Hrochovi za cenné rady, trpělivost a oporu během zpracování této závěrečné práce. Další velké poděkování patří mému konzultantovi Jean-Paul Breuerovi, který byl vždy ochoten pomoci při zpracování podkladových dat. A na závěr bych také ráda poděkovala Norbertu Wernerovi a celému jeho výzkumnému týmu vysokoenergetické astrofyziky za velkou oporu a motivovací při psaní práce.

Prohlašuji, že jsem svou bakalářskou práci napsala samostatně a výhradně s použitím citovaných pramenů. Souhlasím se zapůjčováním práce a jejím zveřejňováním.

V Brně dne

Eva Kosová

Contents

Introduction	1
1 Active galaxies	2
1.1 Radio galaxies	3
1.2 Unified model of AGN	3
1.2.1 Black Holes	4
1.2.2 Accretion disk	4
1.2.3 Jets	4
1.2.4 Molecular toroid	4
1.3 M87 (NGC 4486)	5
2 Jets properties	7
2.1 Formation of jets	7
2.2 Synchrotron radiation from relativistic jets	9
2.3 Structure and dynamics	10
2.4 Relativistic beaming	10
2.5 Super-luminal motion	11
3 Chandra X-ray observatory	14
3.1 Advanced CCD Imaging Spectrometer	15
3.2 High Resolution Camera	15
3.2.1 Operational principles	15
4 Data collection and processing	18
4.1 Reprocessing raw datasets	19
4.2 Clearing and preparing datasets	19
4.3 Correcting absolute astrometry	22
4.4 Difference maps	24
4.5 Technique description of detecting the superluminal motion	27

4.5.1 Knot Hst-1	29
5 Results	30
Bibliography	36

Introduction

For the past couple of decades, astrophysicists have discovered a strong X-ray and radio emission coming from our Milky Way and outer space. The first observations of today's called active galactic nuclei (AGN) were done by Ernest Rutherford in 1908 ([Blandford R. 1999](#)) when he observed strong emission lines at the galaxy NGC1068. This finding was followed by the detection of an optical jet in M87 by H.D. Curtis in 1913. A few years later, the activity of AGN in the Milky Way has been noticed when Karl Jansky discovered the first astrophysical radio emission coming from the center of our Galaxy ([Brittain, J.E. 1984](#)). Unfortunately, astronomy in that time was, above all, optical, so no one paid any attention to these crucial discoveries. That all changed after the Second World War, which led to a swift improvement of radio technology.

Nevertheless, X-ray astronomy was not falling behind, and after detecting the X-ray emission from Sun's corona, the astronomers begin to search for X-ray sources from above Earth's atmosphere. In the beginning, the detectors were placed only on-board of rockets, which were then replaced by the Uhuru satellite launched in 1970 ([Britannica 2019](#)).

Meanwhile, in the late 1950s, in radio astronomy, a groundbreaking observation has been done. A group of astronomers in California obtained a spectrum of the source 3C 273, which was not comparable to any spectrum observed before. The spectral lines did not correspond to any known atomic transition, despite the object's star appearance. It took some time to find out that these mysterious lines match the hydrogen lines with redshift $z = 0.158$. These sources were placed into the category of "quasi-stellar radio sources," later shortened as "quasars," was discovered. With these revelations, the new high-energy astrophysical era has started.

Chapter 1

Active galaxies

Most of the galaxies we observe in our universe are considered normal – the light comes from the stars in visible wavelengths, and is uniformly distributed throughout the galaxy. On the other hand, active galaxies emit up to thousands of times more energy, mostly from their central part. Their power is released in high frequencies ($30 \cdot 10^{15}$ Hz – $30 \cdot 10^{18}$ Hz), thus making them almost unrecognizable from normal galaxies with an optical equipment.

There are four main types of an AGN in active galaxies; we can see their classification in Table 1.1. For comparison, our Milky Way with luminosity $\sim 10^{44}$ erg/s doesn't even get close to the lower limit of blazars and quasars powerful luminosities. Nevertheless, the main focus of this thesis will be put in X-ray on galaxy M87.

Class	Host galaxy	Radio emission	Lines	Luminosity [erg/s]
Blazar	E	strong	weak	$10^{45} - 10^{49}$
Radio-loud Q	E	strong	broad	$10^{45} - 10^{49}$
Radio-quiet Q	S/E	weak	broad	$10^{45} - 10^{49}$
Radio galaxy	E	strong	narrow	$10^{43} - 10^{45}$
Seyfert 1	S	weak	broad	$10^{43} - 10^{45}$
Seyfert 2	S	weak	narrow	$10^{43} - 10^{45}$

Table 1.1: The main properties of the most important types of AGN. In the column *Class* the letter Q stands for quasar and in the column *Host galaxy* the letter E stands for elliptical, and S for spiral galaxy. (Rosswog S. & Brüggén M. 2011)

1.1 Radio galaxies

Radio galaxies can be divided into two general groups. The classification is given by the distance between the regions of highest surface brightness on opposite sides of the central galaxy. Both types are named after astronomers Bernard Lewis Fanaroff and Julia Margaret Riley, who first noticed the connection between distance and luminosity of jets (*Fanaroff–Riley type I, II*). Messier 87 can be assigned as type FR II because the collimated jets in this category often show bright hot spots.

The galaxy’s radio emission can come from the nucleus or a pair of lobes stretched far on both sides. There is a known relationship between the radio core luminosity and the X-ray luminosity. That is why we can also process significant X-ray data from the radio galaxies.

1.2 Unified model of AGN

Massive galaxies hosts powerful engines in their cores called the active galactic nucleus (AGN). It represents the central few parsecs of an active host galaxy. Despite such small dimensions, an AGN produces a tremendous amount of energy, aside from two oppositely directed beams (see Figure 1.1), strong Doppler-broadened emission (in radio), bright cores (in UV and optical), etc.

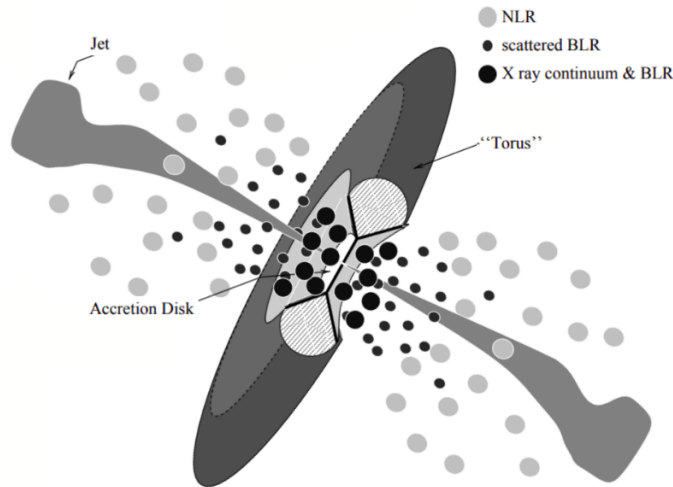


Figure 1.1: The unification model of AGN: The classification of the source depends on the orientation (Sauty C. et al. 2001).

1.2.1 Black Holes

With today's advanced observational techniques, we can say with great redundancy, that there are supermassive black holes in the center of active galaxies with masses of 10^6 to $10^{10} M_{\odot}$. All evidence comes from the dynamic signature of AGNs, specifically from the surrounding stars and gas.

When the first AGNs with supermassive black holes were discovered, they varies greatly in appearance. Moreover, because of that, in the late 1970s, astronomers developed a unified theory. The unified model (see Figure 1.1) says that supermassive black holes are all of the same basic structure; we only see them from different angles and over different periods of time ([Four Peaks Technologies 2012](#)).

1.2.2 Accretion disk

The active galactic nucleus is hiding a supermassive black hole at the center with mass from $10^6 M_{\odot}$ to $10^{10} M_{\odot}$. Objects as massive as this causes a circulation of the surrounding matter. We expect the chaotic accreting particles to collide between themselves, and eventually, all matter will orbit in a single plane that we call an accretion disk. Because the gravitational potential of the black hole dominates, the gas is circling near the Keplerian like orbits.

With the presence of the accretion disk, we may take into account oscillation modes, which can be responsible for AGN's variability over time; nevertheless, it is still a theory in progress. ([Rosswog S. & Brüggen M. 2011](#))

1.2.3 Jets

Astrophysical jets are classified based on their origins to stellar jets and galactic jets. Galactic jets, are believed to have a single source – a supermassive black hole at the center of the galaxy ([Swinburne University of Technology n.d.](#)). These engines are still a mystery for an astronomic community. However, there are some adequate theories about their formation (more details in Chapter 2).

1.2.4 Molecular toroid

One of the unified model's primary components, and the critical insight of why accretion models depend on orientation, is a torus made of a dust and molecules. This dust cloud surrounding the supermassive black hole and the accretion disk must be large enough to cover the whole broad line region from one point of

view, but at the same time, it must be small enough not to overshadow of a narrow-line region.

1.3 M87 (NGC 4486)

Messier 87, also called NGC 4486 or Virgo A, is a giant elliptical galaxy discovered by Charles Messier in 1781 ([Iafrate G. & Ramella M. 2015](#)). He cataloged his discovery as nebula into *The Messier catalog* together with 103 other objects. The galaxy contains a supermassive black hole with a mass of about 3.5 billion Suns and approximately 15 thousands globular clusters; 100 times more clusters than in our Milky Way. Nowadays, the galaxy can be observed in multiple wavelengths, including optical, radio, or X-ray (see [Figure 1.2](#)).

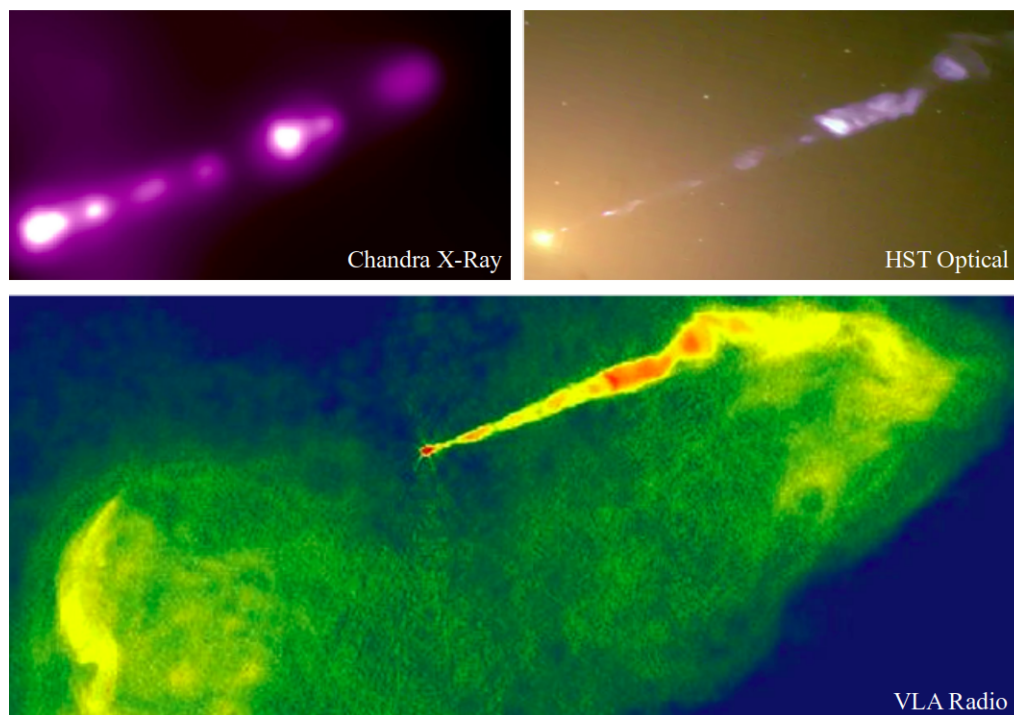


Figure 1.2: View of M87 in a different wavelenghts. Images are taken from [Nimiroff R. & Bonnell J. \(2001\)](#), [Sokol Joshua \(2017\)](#) and [National Science Foundation \(1999\)](#).

In April 2017, astronomers revealed the first image capture ever of a black hole, which was located in the galaxy M87 (see [Figure 1.3](#)). Following this mind-

boggling release, another remarkable view of this galactic center was revealed – how the magnetic field behaves close to the black hole. Jason Dexter, the coordinator of the Event Horizon Telescope Theory Working Group, said that: 'The polarized images mark important steps towards learning more about the gas near the black hole, and in turn how black holes grow and launch jets' (EHT Collaboration 2019). Accordingly, these images could lead to the correct answers about the extragalactic jet formation and the black holes principles on gass feeding and growing.

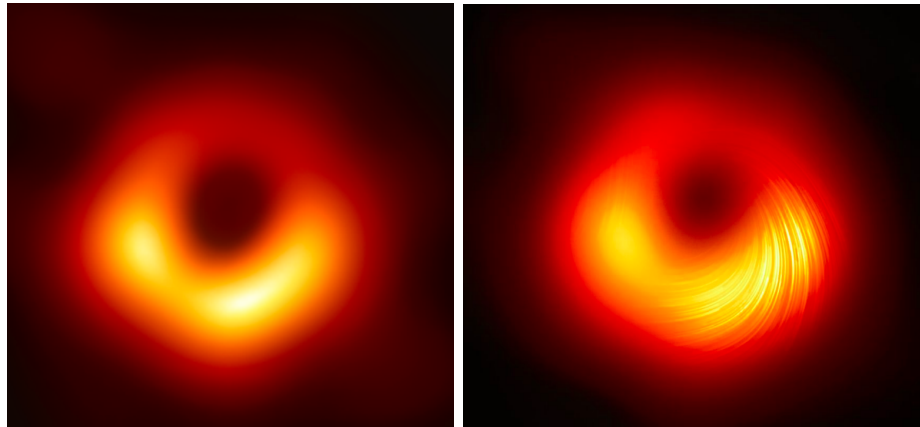


Figure 1.3: The first image of a black hole (on the left) (Castelvecchi D. 2019) and first polarized view of a black hole (on the right) (EHT Collaboration 2019).

Some astronomers also believe that the M87 could have formed from the merge of two or more galaxies and therefore have a companion black hole at the center (Safarzadeh M. et al. 2019).

Chapter 2

Jets properties

The key questions for understanding the physics and role of jets in AGN, and their structure, are related to plasma behavior near the central black hole. Explicitly, we need to know the initial acceleration, how the particles behave when they are moving away from the central region, the connection of the source and plasma itself, the transmission of angular momentum, and how the particles correspond to the magnetized rotating black hole. (Sauty C. et al. 2001)

2.1 Formation of jets

There are four known models of jet formation today (Thorne Kip 1994). The first model, the simplest one, assumes that we have an accretion disk and a space with cold gas surrounding the central part of an AGN, which contains a hot gas. This hot gas pushes the cold gas away from the center, and it will be escaping in the form of jets. However, the colder gas is rotating too. Therefore it will be pushed by the hot gas away just above and below the accretion disk (see Figure 2.1).

The accretion disk in the second model has a temperature of about 10^5 K. This high temperature causes a tunnel shape, very thick proportions of the disk near the central black hole and directs the flowing wind away from the disk. The exact process occurs on the Sun's surface - the solar wind is blown away because of its star's high temperature. In this scenario, jets are forced to escape in two opposite directions (see Figure 2.1).

The third model, first with the magnetic field, presents an AGN structure with magnetic field lines frozen into the accretion disk and the incoming plasma. The field lines are sticking out similarly to the collimated jets in the previous

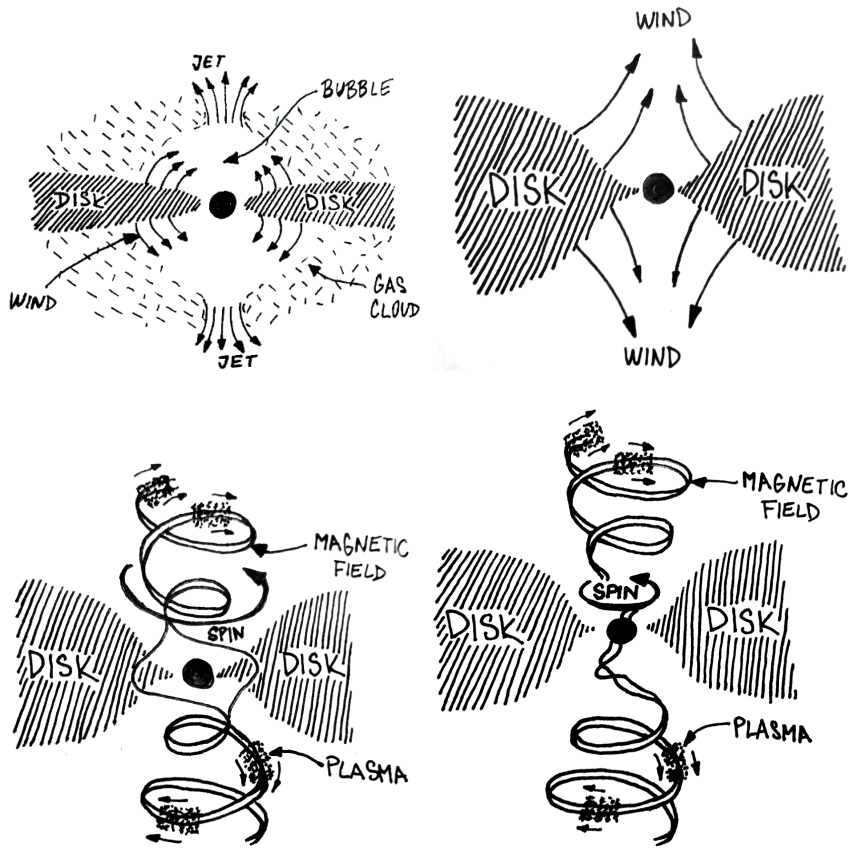


Figure 2.1: Models of jet formation. The simplest model (upper left). Wind model (upper right). First model with magnetic field (bottom left). The most accurate model (bottom right) (own illustration).

model. On the other hand, in this case, the field lines will be affected by centrifugal force, which will rotate these lines, and they will be forced to accelerate. The outgoing plasma will feel the decrease in gravitational forces and will also be tremendously accelerated (see Figure 2.1).

The most accurate model is the last one. It considers magnetic field lines frozen into the accretion disk in the beginning, but over time, the disk's material, along with the magnetic field lines, falls into a black hole. After this happens, the field lines will be coming out from the black hole itself. If the hole is spinning, the lines will be forced to rotate simultaneously. The frozen field lines, and the spinning black hole itself, are accelerating the outgoing material, sliding along

the magnetic field lines upwards and downwards, forming two collimated jets (see Figure 2.1). Therefore, the relativistic jets are formed genuinely due to the black hole spin. This fact might answer the question of why some AGNs are developing jets when others are not.

Still, the jet formation is not considered to be well understood as we have limited knowledge of possible energy sources from which jets are emitted. However, we believe this source can be either an accretion disk or a rotating black hole (Semenov V. et al. 2004).

2.2 Synchrotron radiation from relativistic jets

Through years Chandra observations exposed bright X-ray hotspots and knots in a certain amount of extragalactic jets (Aharonian F. A. 2002). The primary evidence of the synchrotron radiation from these jet's features is the non-thermal spectrum. This type of radio emission occurs when a charged relativistic particle encounters a region with a strong magnetic field – the particle is accelerated along the magnetic field lines and emits electromagnetic radiation during the process (see Figure 2.2). The result is a characteristic spectral shape in the range from radio to near-infrared and optical frequencies (Davelaar J. et al. 2019).

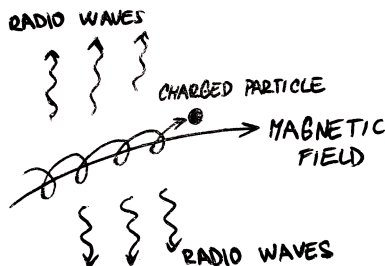


Figure 2.2: The synchrotron radio emission emitted by charged particle inside a magnetic field (own illustration).

Relativistic jets are known to provide very efficient acceleration of relativistic particles up to Lorentz factors $\gamma \sim 10^6 - 10^7$ or higher (Fleishman G. D. 2006). The synchrotron radiation suggests the presence of electrons in the jets, mainly because the synchrotron power $\sim B^2/m^2$ and the magnetic field required for a proton would be extremely high. Compared with laboratory X-ray generators, synchrotron radiation is almost like a laser beam.

2.3 Structure and dynamics

The structure of jet downstream of knot HST-1 can be characterized by several bright spots, blobs (see Figure 5.1) and by highly polarized spiral filaments (Perlmán E. S. et al. 1999). We can expect that the magnetic field will play a significant role in the jet’s structure and its dynamics due to these discoveries.

As the jet pushes its way out of the galaxy center, material at the jet’s tip that is moving through the intergalactic medium causes primary shock ahead. Consequently, the material is decelerated by medium and cannot move as fast as the material near the source. The process will form a reverse shock that proceeds against the original jet’s motion. Further shocks can be developed in the jet because of changes in the extragalactic medium, or jets speed variation.

Motion of jets particles in M87 are associated with both acceleration modes, forward and reverse. For example, knot A and B are believed to be features with reverse mode and knot C with forward mode (Nakamura M. et al. 2010).

2.4 Relativistic beaming

Moving particles in the jets can emit relativistically enhanced radiation as they approach the observer. This effect is called relativistic beaming or Doppler boosting. Strong relativistic beaming is believed to explain the significant brightness variations and high polarization in radio-loud AGNs.

Consider relativistic bulk with a rest-frame velocity $v = \beta c$, corresponding to Lorentz factor $\gamma = 1/\sqrt{1 - \beta^2}$, and the orientation angle, towards the observer line of sight, θ , with defined Doppler factor $\delta = 1/[\gamma(1 - \beta \cos \theta)]$ (Singal A. K. 2016).

Due to the well known Doppler effect, the wave moving towards the observer is seen to have higher apparent frequency (shorter wavelengths). Since, the frequency ν is proportional to the energy E ($E = h\nu$) and the luminosity L is defined as emergent energy per frequency, the apparent luminosity $(L_\nu)_{\text{app}}$ will be boosted by the Doppler factor δ as:

$$(L_\nu)_{\text{app}} = L_{\nu_0} \delta^p, \tag{2.1}$$

where L_{ν_0} is intrinsic luminosity and parameter p describes the source geometry: for moving, isotropic jet $p = \alpha + 3$ (our case with M87), and for continuous jet $p = \alpha + 2$, where α contains an information about the observed integrated spectrum.

The Doppler factor is strongly dependent on viewing angle θ , which gets stronger for smaller angles – enhances radiation of the particles coming towards us, and decreases radiation with opposite direction. At a certain viewing angle at which the relativistic beaming can no longer be neglected is called the critical angle θ_{crit} (see Figure 2.3). The θ_{crit} is estimated individually for different sources; one depends on the β_{app} parameter (see Equation 2.3). Since the jet in M87 is deviated from the line of sight by $\theta = 17^\circ$ and the critical angle at which apparent velocity is maximized is $\theta_{\text{crit}} \geq 22^\circ$ (Walker R. C. et al. 2018), Doppler boosting effect has to be taken into account in calculations of superluminal motion.

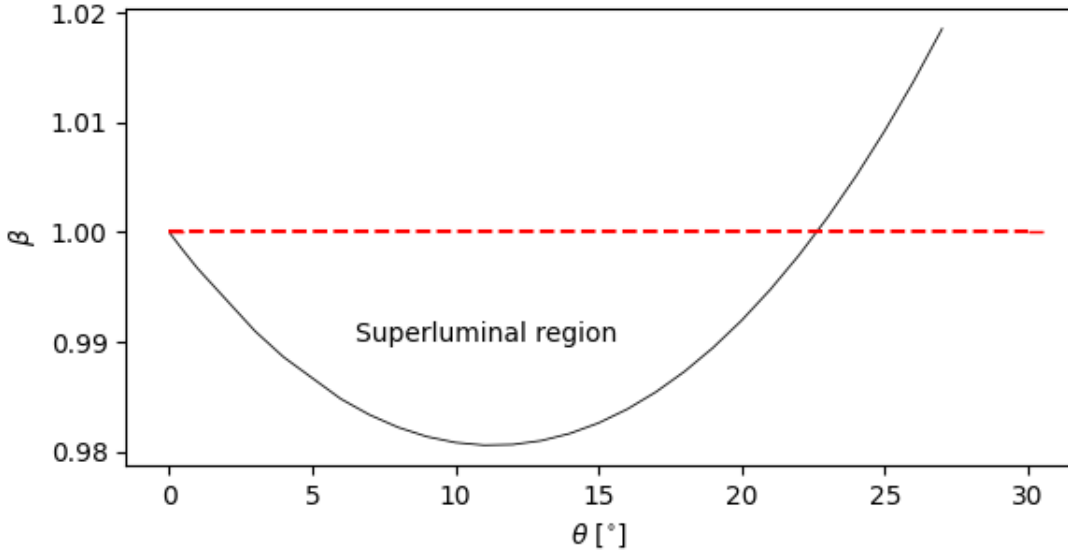


Figure 2.3: The dependence of velocity β on the viewing angle θ . Parameter β_{app} from equation 2.3 is set to 5 to match the limit of M87 (own illustration).

2.5 Super-luminal motion

The motion of jets has been traced by astronomers over a long time period, using the positions of their bright features. In 1966 Martin Rees pointed out that: "an object moving relativistically in suitable directions may appear to a distant observer to have a transverse velocity much greater than the velocity of light" (Rees M. J. 1966). That was a case for many observations of extragalactic jets; however, if this were true, fundamental pillars of the theory of relativity would

fail. Therefore, there had to be another explanation for this unusual phenomenon. The solution is quite simple – a projection effect (see Figure 2.4). To observe changes in the AGN structure, typically, we need a time interval of few months.

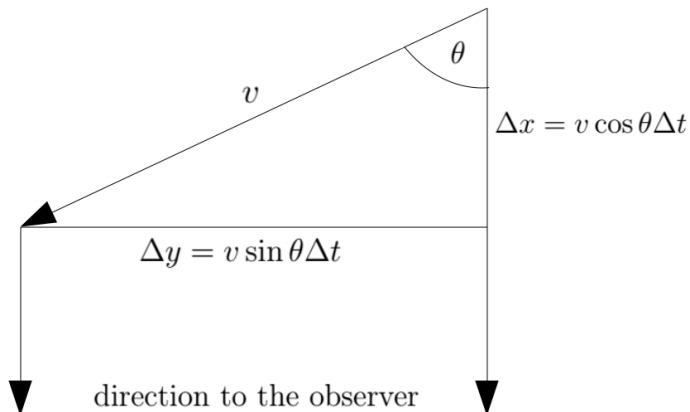


Figure 2.4: The geometry of superluminal motion (own illustration).

In AGNs, the emission is believed to be produced by the synchrotron process (see Section 2.2); components are moving towards the observer with $v \rightarrow c$. Since the core of AGN is assumed to be stationary, its radiation will always travel simultaneously towards the observer.

First of all, we will introduce the well-known relativistic parameter β , which refers to the speed of an object in natural units $\beta = v/c$. We can now imagine part of the material ejected at speed v (near c) and its emitted light with speed c at the angle θ along the line of sight as shown in Figure 2.4. After some time Δt , the material has traveled the distance $\beta \cdot \Delta t \cos \theta$ and the light $c \cdot \Delta t$. The consequence of this "material-light chase" is that the second detected signal is observed with time delay $c \cdot \beta \cdot \Delta t \cos \theta$.

The apparent velocity across the plane of sky is given by the distance traveled by the observed feature Δy (see Figure 2.4) divided by the elapsed time Δt_{el} between two consequent measurements:

$$v_{\text{app}} = \frac{\Delta y}{\Delta t_{\text{el}}} = \frac{\Delta t \beta c \sin \theta}{\Delta t - \Delta t \beta \cos \theta} = \frac{v \sin \theta}{1 - \beta \cos \theta}. \quad (2.2)$$

$$\beta_{\text{app}} = \frac{\beta \sin \theta}{1 - \beta \cos \theta}. \quad (2.3)$$

The resulting formula indicates, that the apparent velocity of moving particles can be higher than the speed of light, if the values of angle θ are small enough (see Figure 2.3). Superluminal motion occurs when the $v_{\text{app}} > c$, and this will happen when $\beta(\cos\theta + \sin\theta) > 1$. With the Chandra satellite we can measure the angular velocity of the moving object $\omega = \Delta\varphi/\Delta t$ and for correct calculations, it is necessary, in the begging, to convert ω to linear velocity v as $v = \omega \cdot d$, where d is the distance to the observed source.

Chapter 3

Chandra X-ray observatory

The Chandra X-ray Observatory is NASA's "Great Observatory" alongside with Spitzer Space Telescope, Hubble Space Telescope, and Compton Gamma Ray Observatory. On July 23, 1999, Chandra was successfully launched into the Earth's orbit ([Howell Elizabeth 2018](#)).

This X-ray telescope was sent to orbit to detect high-energetic photons, which cannot be reflected by mirrors similarly structured as the parabolic mirrors in the optical telescopes. The main reason why it is not possible can be found in the energy of X-ray photons. The X-ray photons are incredibly energetic and would quickly penetrate the telescope's parabolic mirrors. In other words, the X-ray photons cannot be reflected by optics based on the total internal reflection. Consequently, Chandra's technical team constructed a structure with four nested pairs of cylindrical paraboloid and hyperboloid mirrors ([Chandra X-ray observatory 2008](#)). This construction is called High Resolution Mirror Assembly (HRMA) and is one of the primary and necessary components of the Chandra telescope. With this structure, specifically assembled for reflection in genuinely small angles, another complication arises – extreme surface smoothness. The smoothness is done with such precision that if we compare it to the polishing of the Alps in the same relative way as Chandra's mirrors, Mont Blanc would be less than 3 cm tall ([Harvard-Smithsonian Center for Astrophysics 2014](#)). Detailed structure with the extreme smoothness of mirrors provides Chandra to detect 80% – 95% of the incoming photons.

Chandra's trajectory is highly elliptical and allows the satellite to observe through 85% of its entire orbit constantly. Onboard, the satellite carries two microchannel focal plane detectors: Advanced CCD Imaging Spectrometer (ACIS) and High Resolution Camera (HRC) ([Caballero J. A. et al. 2010](#)). Their as-

signment is to record the position and number of incoming X-ray photons, their time of arrival, and lastly, their energy.

3.1 Advanced CCD Imaging Spectrometer

As the title indicates, the structure of this instrument contains series of charged coupled devices (CCDs), more specifically, ten planar CCDs, which are divided between two detectors: ACIS-I (for imaging) and ACIS-S (for spectroscopy). ACIS-I uses only four of the CCDs. The charged devices are sorted into 2×2 array, and all of them are front-illuminated (FI). On the other hand, ACIS-S is working with 1×6 array from which only four CCDs are FI, and the other two are back-illuminated (BI) ([Chandra X-ray Center 2020](#)). This specific arrangement of CCD chips allows us to observe more energy levels since the BI chip has better resolution than the FI chip (FI range = 0.8 – 8.0 keV, BI range = 0.3 – 8.0 keV). The fixed physical size of CCD pixels is a disadvantage to the ACIS's spatial resolution, which is due to that limited to $24.0 \mu\text{m} \sim 0.492 \text{ arcsec}$. Despite this slight issue, the detector can still measure the energy of incoming X-ray photons.

3.2 High Resolution Camera

Like ACIS, HRC is also a device containing two detectors. This time, unlike in the previous instrument, they are CsI-coated microchannel plate (MCP) detectors: HRC-I (for imaging) and HRC-S (for spectroscopy). The HRC-I is an optimized detector for imaging and has the largest field of view of any other detector on Chandra satellite ($30 \times 30 \text{ arcmin}^2 = 100 \times 100 \text{ mm}^2$). The energy range we can observe goes even beyond ACIS sensitivity, explicitly from 0.08 to 10.0 keV ([Smithsonian Astrophysical Observatory 2021](#)). The unique potential of HRC lies in the focusing power of Chandra mirrors. Combining these two mechanisms can produce highly detailed images with a precision of 0.5 arcsecond ([HS Center for Astrophysics 2019](#)). That is equivalent to the ability to watch a chess game from a distance of 37 km, for example.

3.2.1 Operational principles

For good functionality of the detector, it is necessary to reduce as much as possible incoming UV photons, ions, and low-energy electrons. To filter out unwanted particles, the detector contains a UV/Ion shield places right on the top, allowing

only the energetic X-ray particles to penetrate through it. Once the particles passed through the shield, they get absorbed in the CsI-coated surface placed on the first MCP. Deeper in the HRC-I detector, we can find two MCPs, which consist of 690 million lead-oxide glass tubes that are about $10\ \mu\text{m}$ thick and 1.2 mm long. The tubes are rotated in opposite directions at an angle of 6° (see Figure 3.1).

This structure enhances a probability of an X-ray photon interaction with the tube, which is needed for photoemission. Released electrons are then accelerated by an applied electric field which causes another strike of them into the tube's wall producing secondary electrons, followed by a whole cascade of charged particles.

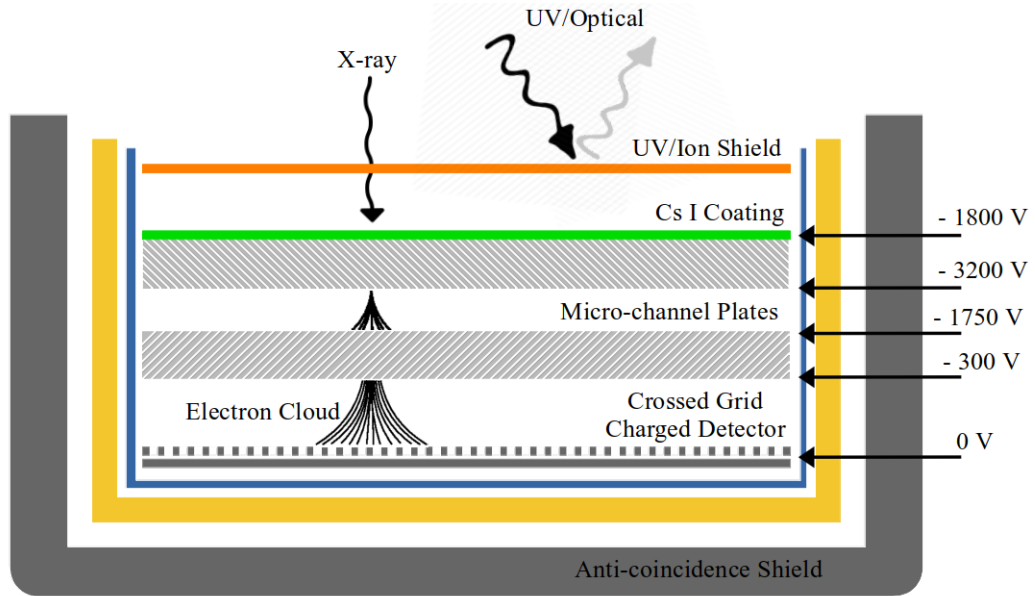


Figure 3.1: A structure of the HRC detector (own illustration).

Now the electrons arrived at the second MCP, aiming to provide additional gain and remove the possible response from positive ions. The positive feedback is eliminated by the reverse tube's inclination, which causes the contact between the tube's walls and ions, resulting in another release of electrons. The electron cloud is accelerated towards a position-sensitive detector where the 'three tap algorithm determines the centroid position of an incoming X-ray photon.'

Despite the sophisticated structure of HRC, sometimes not only X-ray photons can get through the MCPs. Fortunately, the spatial distribution of electrons

leaving the second MCP has a very specific shape for X-ray events – hyperbola. Non-X-ray events often produce more spatially extended and complex distribution. Therefore, it is possible to remove non-X-ray events by simply filtering out those that do not fit the hyperbola shape. ([MSFC Chandra IPI Teams 2020](#))

Chapter 4

Data collection and processing

Galaxy M87 is a nearby source at distance of 16.7 Mpc that host 1.6 kpc long jet, stretched out of the AGN. The jet of M87 is known to be a bright radio, and optical source, with relativistic motion on kiloparsec-scale. In this thesis we will be processing raw data of this extragalactic jet observed by Chandra X-ray satellite from years 2012 and 2017 (see Table 4.1). In the process, we follow the methods and path listed in an article "Detection of Superluminal Motion in the X-ray Jet of M87" written by Bradford Snios (Snios B. et al. 2019). Observations from ACIS was initially considered to be part of this thesis, but due to the shorter exposure times, worse spatial resolution than HRC-I (ACIS ~ 1 arcsec, HRC-I < 0.5 arcsec) and pile-up issues, we could not achieve the required astrometric precision between epochs. Because of that, we focused only on HRC-I observations.

ObsID	Date	Observer	Detector	Exposure time [ks]
13515	2012	Murray	HRC-I	74.31
18612	2017	Kraft	HRC-I	70.56

Table 4.1: Used *Chandra* observations of M87 with corrected exposure time.

All observations were obtained from Chandra Search & Retrieval archive (ChaSeR) (X-Ray center 2021). For analysis, we used the Chandra Interactive Analysis of Observations software package (CIAO software) version 4.12 developed by Chandra X-ray Center (Smithsonian Institution 2021), specifically for X-ray data examination. Individual images were displayed and visualized with *SAOImageDS9* (Center for Astrophysics 2021). For standard data processing and adjusting, CIAO software uses Chandra Calibration Database (CALDB –

version 4.9.2.1 in our case), which have stored and provided access to the required calibration files. For example, if we created an exposure map, applied a gain map, or build response files like RMFs (Response Matrix Files), and ARFs (Ancillary Response Files), we are using the Chandra CALDB.

4.1 Reprocessing raw datasets

In both infraRed (IR) and optical astronomy, the primary data output is an image. On the other hand, in X-ray astronomy, the primary data output is a table of photons or event lists. Right after downloading necessary data from Chandra's *ChaSeR* archive, the event lists are unprocessed, and we have to process them to continue with the analysis. CIAO software has the following command ([Smithsonian Institution 2020a](#)) for reprocessing primary datasets into event files with acceptable processing level = 2 (Levels - 0, 1A, 1B, 2, 3, 4):

```
unix% chandra_repro {ObsID} outdir= verbose=1 clobber=yes
```

The script reads data from both primary and secondary directories (standard data distribution) and creates, moreover, a new bad pixel file and the new level=2 Type II Pulse Height Amplitude file (PHA).

4.2 Clearing and preparing datasets

Individual features in extragalactic jets may, over time, decrease or increase in brightness. To precisely measure flux change in the filaments over time, it is necessary to remove as many background flares as possible, with the least possible distortion of data's statistics which can be useful later on. That can be done by using the CIAO routine `deflare`.

Before we begin with the routine, it is appropriate to stop for a while, and to think about the size of our files. As you can see in [Figure 4.1](#), the studied jet takes only a few percent of the whole event file. By simply cutting a region around the source, we will significantly reduce the size of the processed data, reducing the amount of time CIAO software will spend on processing them. Another thing, we need, is to ensure that level=2 event files will not be overwritten by an accident through the data processing; both can be done by following commands ([Smithsonian Institution 2013b](#)):

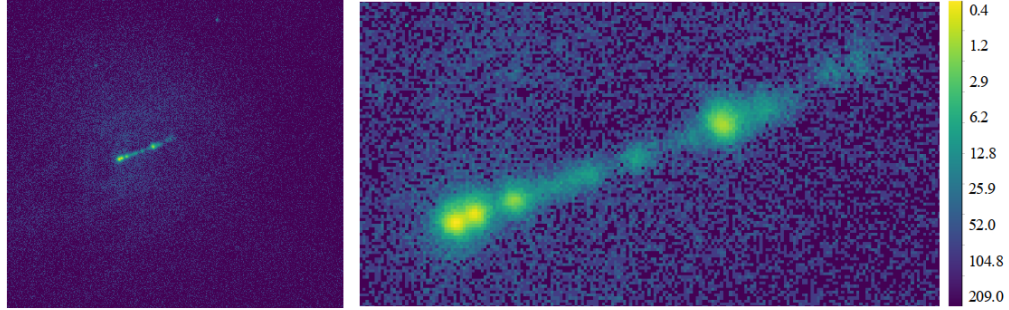


Figure 4.1: Original level=2 image (left) and new trimmed image (right).

```

unix% dmcoppy "evt2.fits[sky=box(s(x),s(y),x,y,fi)]" cutted_evt2.fits
--> works only for event files
unix% dmcoppy "evt2.fits[x1:x2,y1:y2]" cutted_evt2.fits
--> works only for image files

```

Parameters $s(x)$, $s(y)$ are physical coordinates of the rectangular's center, x , y are its lengths on x and y axes in pixels and fi is an angle of rotation of the rectangular around the source. In the second command, $x1$, $x2$, $y1$, $y2$ are physical coordinates of the box section we want to cut.

We have performed all the necessary steps to do the actual background flares filtering with the following script ([Smithsonian Institution 2019](#)) in CIAO:

```

unix% punlearn dmcoppy
unix% dmcoppy "cutted_evt2.fits" evt2_lc.fits

unix% punlearn dmextract
unix% pset dmextract "evt2_lc.fits[exclude sky=region(ds9.reg)]
[bin time=:500]"
unix% pset dmextract outfile=light_curve_fit.fits
--> creates lightcurve fit file with bin time 500 s
unix% pset dmextract opt=ltc1
unix% dmextract

unix% deflare light_curve_fit.fits outfile=deflare_lc.gti
method=sigma plot=yes save=deflare_lc_sigma_plot
unix% punlearn dmcoppy
unix% dmcoppy "evt2_lc.fits[@deflare_lc.gti]" deflared_evt2.fits

```

In the first section of the script, we copy the `evt2` file to keep the original unchanged in our directory and continue the clearing process with the new one. Command `punlearn` restores the default parameter values of CIAO routines. In the middle section of the script we are creating background light-curve fit file with CIAO `dmextract` task. By selecting a region around the source (of any shape) and saving it in CIAO format with physical coordinates into the `'ds9.reg'` file, we can find the background light curve. Using `'opt=ltc1'` is appropriate when one of the specified parameters is a bin time. Normally, the count rate is taken as counts per bin unit per total good observational time. Choosing `opt=ltc1` ensures that the count rate is taken as counts per total time associated with the bin, rather than total time associated with the observation. Part of the `deflare` script is `lc_sigma_clip` routine, which uses an iterative sigma-clipping algorithm to detect and remove points that fall outside the range from $mean - n\sigma$ to $mean + n\sigma$, where default n value is set to 3 (see Figure 4.2). GTI file is the product of the `deflare` script, which can be at the end used for cleaning our dataset.

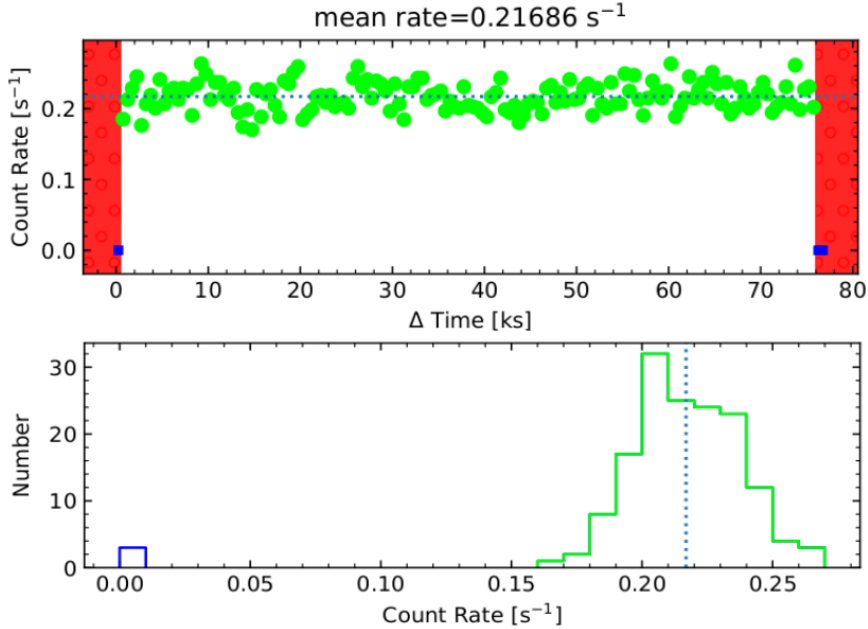


Figure 4.2: Plots from `lc_sigma_clip` clipped at 3σ for obsID 13515. Points in red parts are outside the interval $\pm 3\sigma$

After removing the background flares from our data, the next step is to create

exposure-corrected images and exposure maps of our observations, which will be helpful later on. The following syntax ([Smithsonian Institution 2021](#)) will create 'fluximage' folder with all the listed files above:

```
unix% fluximage repro/deflared_evt2.fits fluxed/ bin=1
```

The binning factor is set to 1 because the default binning value is 32, and for the most accurate calculations of superluminal motion, we want to maintain Chandra's original resolution, which is 0.1318 arcsec/px. For HRC-I observation, the `fluximage` routine creates by default, wide band images with effective energy 1.5 keV.

4.3 Correcting absolute astrometry

Most of the CIAO analysis threads can be removed by `chandr_repro` script. Unfortunately, the absolute astrometry does not fall into that category. Removing the small offset between our datasets is extremely important because of the superluminal motion calculations, a small difference can vastly change the results. As the first step, we determined the center of AGN with two different methods to make sure it was done correctly. We used the horizontal and vertical graphs in *SAOImageDS9* (see Figure 4.3) and then statistical `dmstat` routine in CIAO, with following command line ([Smithsonian Institution 2013c](#)):

```
unix% dmstat "cutted_evt2.fits[sky=circle(cx,cy,r)]" centroid=yes
--> prints out the position with minimum and maximum photons
in the selected region
```

The circle region with parameters cx (horizontal coordinates of center), cy (vertical coordinates of center), and r (radius) is drawn only around AGN. Therefore the CIAO statistics are not mistaken by other filaments in the jet. The results from both methods match, within the accuracy, very nicely, so we can continue with the process.

As a stationary point, which we will use to align both of the observations, will be the supermassive black hole at the AGN center. Many astronomical databases were ingested to get the most accurate determination of the black hole's coordinates. Eventually, they were taken from the STScI Digitized Sky Survey (SDSS)

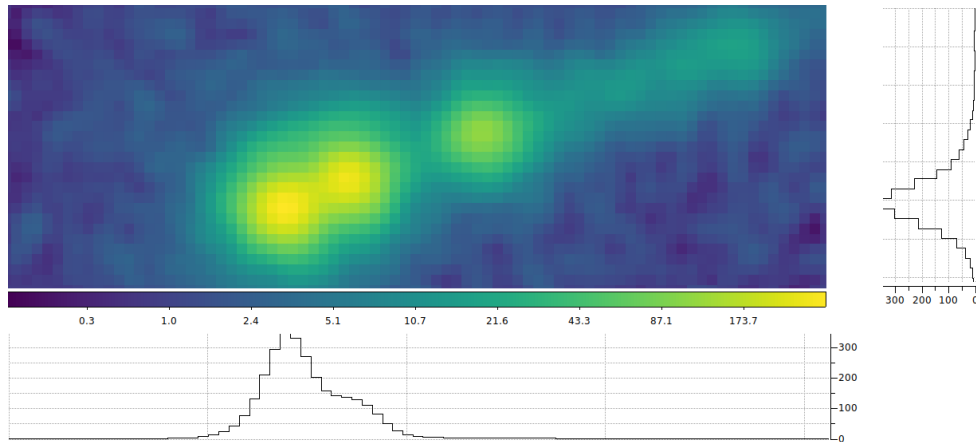


Figure 4.3: Close-up image of the jet’s central part with displayed graphs from *SAOImageDS9*, which measure the total counts in the x and y directions.

archive using *SIMBAD* database as the optical position listed by the SDSS varies within 0.1 arcsec with *Gaia* Catalog (Graham A. W. & Soria R. 2019).

At this point, we determined the photometric center of AGN in both epochs and selected the best coordinates of the black hole that fits our observations. The offset was now corrected by CIAO task `wcs_update` (Smithsonian Institution 2013a):

```

unix% dmcopu cutted_evt2.fits corrected_evt2_2012.fits op=all
-->  copies all parametres from "cutted_evt2.fits" file into
      new "corrected_evt2_2012.fits" file
unix% wcs_update infile=corrected_evt2_2012.fits wcsfile=wide_thresh2017
      .img deltax=dx deltay=dy

```

Parameters dx and dy are the differences in the physical coordinates between our determined AGN center and known coordinates of the supermassive black hole in M87. Since the shift can be applied only to one file, and our control World Coordinate System file (WCS) is set to be from year 2017, the changes will be applied to the file from 2012. Chandra’s software CIAO offers multiple options for correcting absolute astrometry. One of them – specifically the `wavdetect` routine – was initially considered for the process. Although this method can be less affected by a systematic error, since it runs without human interaction, it could not achieve the same accuracy as the technique mentioned earlier.

We tested the systematic error in the first method, and the AGN position was found to agree within the interval $0.0076 - 0.0043$ arcseconds between the epochs. Since the proper motion in M87 at speed c would produce a total shift of 0.019 arcseconds over five years (Snios B. et al. 2019), and the previous observations show superluminal motion greater than $6c$, we concluded that the images are coaligned precise enough for this analysis.

4.4 Difference maps

At first sight, when we look at the extragalactic jet in M87, we notice notable changes in brightness and morphology of individual knots between the two epochs (see Figure 4.4).

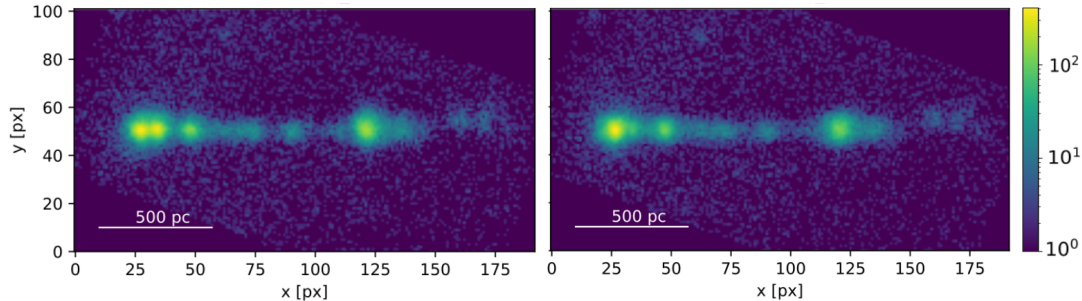


Figure 4.4: Rotated images of jet from both epochs. Observation from year 2012 is on the left and from 2017 is on the right.

Using modified and coaligned images from previous sections, we were able to create a difference map of the two epochs (see Figure 4.5) and calculated the pixel signal-to-noise ratio (S/N) between epochs as followed:

$$S/N = \frac{|e_2 N_2 - e_1 N_1|}{\sqrt{e_1^2 N_1 + e_2^2 N_2}}, \quad (4.1)$$

where the N_1 and N_2 are representing number of raw counts for every pixel in each epoch and e_1 , e_2 are the corresponding exposure durations.

For the computational manipulation of the pixels, and header information in the files, the images need to have the same dimensions. In our case, we set the image proportion to 190 pixels on horizontal axes and 100 pixels on vertical axes. The final image was constructed with CIAO software using `dmimgcalc` routine (Smithsonian Institution 2020b) with following syntax:

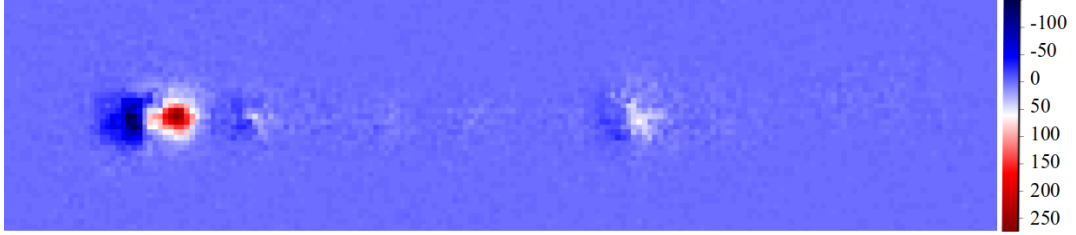


Figure 4.5: Difference map, where the red and white regions correspond to brighter areas in the 2012 dataset and the darker blue regions to brighter areas in the 2017 dataset.

```

unix% dmimcalc "corrected_evt2_2012.fits,corrected_evt2_2017.fits"
signal_to_noise.fits op="imgout=(fabs((img2*img2_exposure)-(img1*img1
_exposure)))/(sqrt((img1_exposure*img1_exposure*img1)+(img2_exposure
*img2_exposure*img2)))"

```

The $img1/2_exposure$ parameters are taking values from the 'EXPOSURE' row in the image's header. At this point, it is necessary to define individual knots in the jet. We used *SAOImageDS9* visualization to determine eight features with radius < 1.1 arcsec with the program's linear scale contour rendering. Each feature is presented in Figure 5.1. The center of shown circle regions were found with CIAO *dmstat* routine for the best possible statistical results.

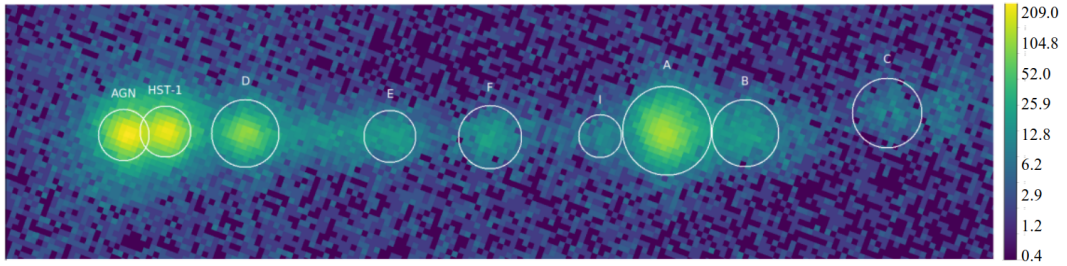


Figure 4.6: Jet's image from year 2012 with marked regions around features.

In addition, we generated the integrated S/N map, or in other words, integrated squared residual R per region:

$$R = \sum_i^{N_p} (S/N)_i^2, \quad (4.2)$$

where $(S/N)_i$ is the S/N previously calculated in equation (4.1) for the i th pixel and N_p is the total number of pixels in the selected region. To obtain the N_p parameter, we need to construct the image of R using once more `dmimgcalc` task:

```
unix% dmimgcalc "signal_to_noise.fits" residual_image.fits op="imgout=
img1*img1"
```

The values of integrated squared residual are vital because they could reflect changes in the brightness of a jet feature, changes in the position, or both. Unfortunately, the original files we used for the calculations of pixels with zero counts. Consequently, the resulting images contained NaN value pixels. These pixels could cause irregularities in later calculations; therefore, it is essential to remove them. This process cannot be done with a specific routine in CIAO. Therefore we have to write an original script for that task. As a scripting language, I choose *Python*, mainly because we practice this language in multiple lectures at my alma mater Masaryk University, and because, it is a very intuitive language to work with.

Before we start, we need to do one more thing. The Python `astropy` package we will be using works only with image fits files, and we are working with event files from the beginning. Fortunately, CIAO software is capable to convert these event files to images with the following command:

```
unix% dmcoppy 'deflared_evt2.fits[EVENTS]' evt2_image.fits option=image
```

The CIAO syntax will create a new image file, which we can now modify in *Python* as follows:

```
import numpy as np
import astropy.io.fits as astro
from astropy.convolution import Gaussian2DKernel,
    interpolate_replace_nans

filename1 = 'HRC/deflared_images/signal_to_noise.fits' #S/N
filename2 = 'HRC/deflared_images/squared_residual.fits' #R

fits1 = astro.open(filename1)
fits2 = astro.open(filename2)
im1 = fits1[0].data
```

```

im2 = fits2[0].data

im1[im1 < 0.00000001] = np.nan # mask over pixels with low counts values
im2[im2 < 0.000000000000001] = np.nan
kernel = Gaussian2DKernel(x_stddev=1)
# Smooth the masked pixels with a 2D Gaussian in a 9x9 arrays

fixed_image1 = interpolate_replace_nans(im1, kernel)
fixed_image2 = interpolate_replace_nans(im2, kernel)

```

After the application of these required proceedings, we got the resulting images, which are entirely prepared for later analysis (see Figure 4.7).

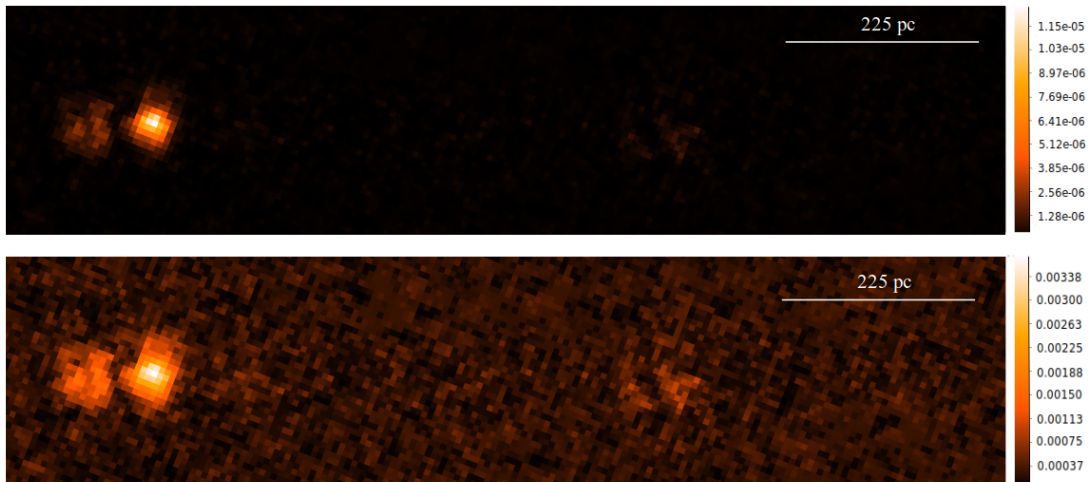


Figure 4.7: Squared residual image (upper) and signal to noise image (lower) without NaN value pixels.

4.5 Technique description of detecting the superluminal motion

Chandra’s exceptional resolution should allow us the reveal of evidence of the proper motion in the jet of M87, whose values can reach up to $6c$. In this thesis, we considered multiple methods for calculatins of the superluminal motion. First, we tried to determine it using contours in *SAOImageDS9*. We can adjust four

parameters in the contour analysis window in the tool: the number of isophotes (levels), the smoothness, and the fluxes of the lowest and highest contour. Some common drawback with this method have already occurred during the parameters adjustment. If we look at Figure 4.8, the first image (on the left side) looks much more evident than the second one (on the right), and we can comfortably recognize individual features in the jet. However, if we wanted to measure superluminal motion from these contours, the errors would have been enormous due to the dimensions of the central shapes. On the other hand, the central regions in the second image are much smaller and better defined. Nevertheless, the parameter settings here are at the edge of HRC-I pixel resolution, as you can see, especially at the ages of the second image (contouring around single pixels). To improve the contours, we tried many more combinations of parameters, but none reach the criteria for accurate computation of proper motion.

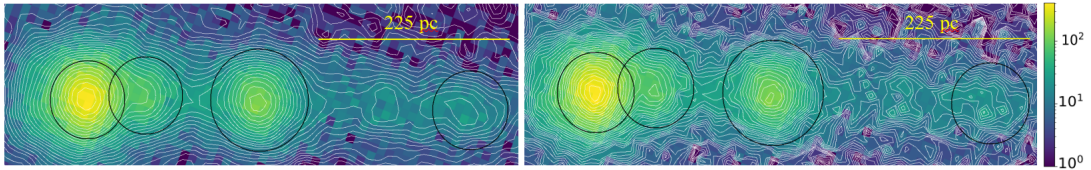


Figure 4.8: Close-up images of AGN and knots HST-1, D, and E from the year 2017 with contours; the contours differ in smoothness and number of levels; smooth = 3 and levels = 40 (left image), smooth = 2 and levels = 50 (right image).

The second method, we tried, was simply statistical. The photometric center and the center, standard error of individual feature, were calculated with CIAO software using `dmstat` task as follows:

```

unix% dmstat "ObsID/repro/corrected_evt2.fits[sky=circle(cx,cy,r)] [bin
sky=1]" centroid=yes
--> for center
unix% dmstat "ObsID/repro/corrected_evt2.fits[sky=circle(cx,cy,r)] [bin
sky=1]" centroid=no
--> for standard error

```

The centroid position, \bar{x} , is defined as the count-weighted mean:

$$\bar{x} = \sum_{ij} \frac{n_{ij}x_{ij}}{N}, \tag{4.3}$$

where n_i is the number of events in the i th pixel, x_i is the pixel's position, and N is the total event counts for a given region. The standard deviation of the center, from which the superluminal motion errors will be determined, is estimated as:

$$\Delta x = \sqrt{\frac{1}{N(N-1)} \left(\sum_{ij} n_{ij} x_{ij} - \bar{x} \right)^2}. \quad (4.4)$$

4.5.1 Knot Hst-1

In the previous section, specifically in the difference map, we can see the HST-1's enormous variety in brightness. Due to its close proximity to the AGN and this vast change in brightness from 2012 to 2017, we were unable to establish the centroid location accurately enough for superluminal motion's calculation. Therefore we had to modify our previous method to determine the exact position of HST-1 knot.

To begin, we extracted 3.157×3.157 arcsec region around the HST-1 and AGN from both epochs and save it as 'AGN_HST.fits'. For greater accuracy, we binned both observations at the subpixel size 0.066 arcsec/px using `fluximage` routine in CIAO:

```
unix% fluximage repro/AGN_HST.fits AGN_HST_0066/ bin=0.5
```

Additionally, we tried binning at 0.25, which would give us pixel size 0.033 arcsec/px. However, the resulting image were too scattered for deeper analysis, thus we continued the process with images binned with factor 0.5.

Chapter 5

Results

In the first part of our work, we focused on the difference in brightness of individual features observed in the jet. We measured total flux for each epoch emitted over the 0.08 – 10.0 keV energy band in determined regions around filaments (see Figure 5.1). The changes between the two epochs were defined as $(F_{2017} - F_{2012})/F_{2012}$, where F is the found flux (see Table 5.1). Positive values in the "Change in Flux" column indicate an increase in brightness in 2017, and negative values indicate a decrease. Uncertainties were determined using the propagation of errors formula with multiple variables.

Feature	R/N _p [(S/N) ² /px]	Flux [10^{-5} photon cm ⁻² s ⁻¹]		Change in flux [%]
		Epoch 2012	Epoch 2027	
AGN	444.75/66	75.20 ± 0.72	96.30 ± 0.87	28.06 ± 1.69
HST-1	3071.72/64	70.85 ± 0.58	25.67 ± 0.25	-63.77 ± 0.46
D	175.90/108	30.67 ± 0.22	33.97 ± 0.24	10.76 ± 1.12
E	90.37/67	5.65 ± 0.03	4.93 ± 0.04	-12.74 ± 0.85
F	129.84/96	6.09 ± 0.04	5.56 ± 0.03	-8.70 ± 0.78
I	66.29/46	2.31 ± 0.02	2.35 ± 0.03	1.73 ± 1.57
A	562.61/191	62.84 ± 0.29	56.83 ± 0.24	-9.56 ± 0.56
B	96.42/107	8.96 ± 0.04	8.59 ± 0.04	-4.13 ± 0.62
C	138.39/116	3.08 ± 0.02	3.09 ± 0.02	1.00 ± 0.92

Table 5.1: Complete analysis of jet's X-ray brigtness in both epochs.

The values of squared residual overall are consistent with the change in brightness of jet features, as we predict in section 4.4. The most significant decrease in brightness was found in knot HST-1, while the most increase in brightness was

observed in the AGN. In the remaining knots, the variation in brightness is not nearly as significant. However, the values are still consistent with the difference map and squared residual values.

In the following part, we aimed to calculate proper motion differences of the studied jet. As we mentioned in the previous chapter, the center location of the HST-1 knot was determined differently from the remaining knot's position. The modified images with the improved resolution are presented in Figure 5.1. The upper images are from the year 2012 and the lower from the year 2017. The dashed white lines illustrate the center position of knot HST-1, while the green lines represent a supermassive black hole at the center of the observed galaxy.

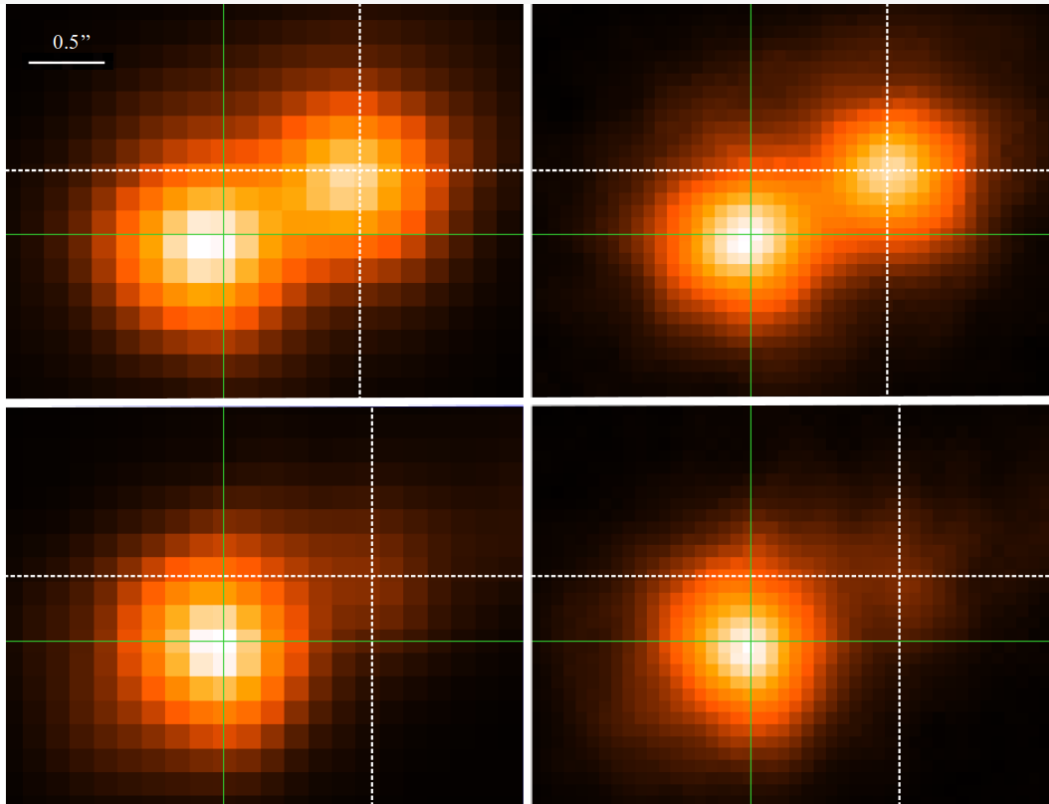


Figure 5.1: Comparison of M87 core and HST-1 with Chandras original resolution (left column) and modified image with subpixel size 0.066 arcsec/px.

Based on the detected change in position of the HST-1 knot from Figure 5.1, we can assume the presence of the superluminal motion. We are now at the point where all the center positions of features are established, including the precise

static location of AGN. Therefore, we can find precisely enough the distances between AGN and individual filaments in the *SAOImageDS9*. Since the knots can move in the parallel and perpendicular direction in terms of the jet axis, we need to consider both of the options. The shift in perpendicular direction (Δ_{\perp}) was determined from the angle between feature, AGN, and jet axis φ (see Figure 5.2) and the shift in parallel position (Δ_{\parallel}) was calculated as $D_{2017} - D_{2012}$.

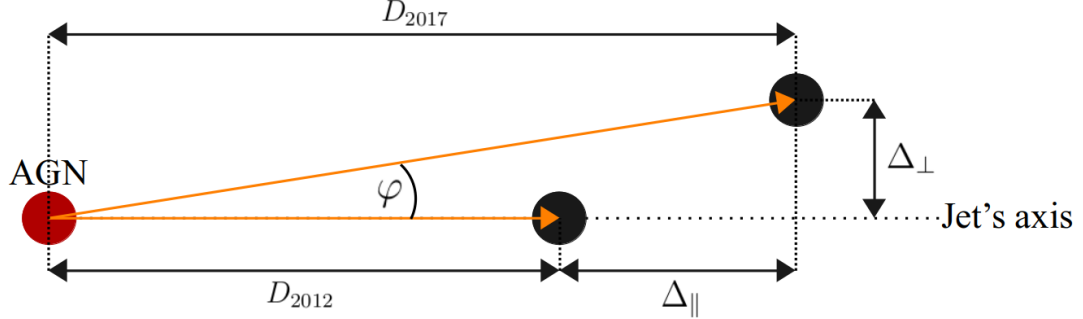


Figure 5.2: Scheme for calculations of parallel and perpendicular shift of moving feature in the jet (own illustration).

The results are shown in Table 5.2, where negative values represent reverse movement in the parallel direction or movement down below the jet axis.

Feature	Distance		Shift [pc]		$\beta_{\text{app},\parallel}$ [c]	$\beta_{\text{app},\perp}$ [c]
	[arcsec]	[kpc]	Δ_{\parallel}	Δ_{\perp}		
HST-1	0.94	0.08	5.75	0.21	6.57 ± 1.82	0.15 ± 0.56
D	2.78	0.23	1.46	-0.11	3.33 ± 0.77	-0.07 ± 0.23
E	6.05	0.49	0.49	-0.44	1.11 ± 0.93	-0.31 ± 0.29
F	8.30	0.67	0.49	-0.32	1.11 ± 0.85	-0.22 ± 0.26
I	10.89	0.88	0.81	0.80	1.85 ± 0.61	0.56 ± 0.19
A	12.44	1.01	1.05	-0.32	2.41 ± 1.76	-0.22 ± 0.54
B	14.25	1.15	0.32	0.40	0.74 ± 0.97	0.28 ± 0.30
C	17.51	1.42	0.40	1.93	0.93 ± 0.78	1.35 ± 0.24

Table 5.2: Proper motion for X-ray knots in jet of M87.

In addition, we analyzed the dependence between measured errors in pixels and resulting errors in superluminal motion (see Figure 5.3). The dashed line at the bottom represents the maximal calculated error in this thesis. From the

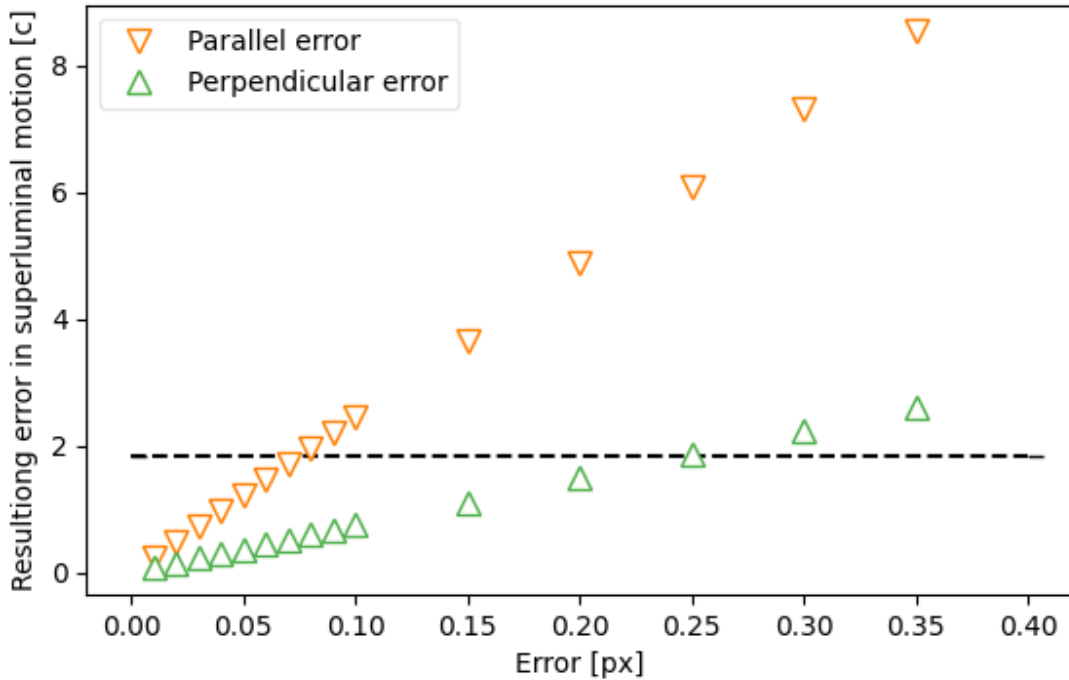


Figure 5.3: Errors in superluminal motion caused by measured pixel error.

graph 5.3 we can see that the dependency connecting the two parameters is linear.

The last and final step in our work was to determine the proper motion of each feature in the jet. The results of knots movement are shown in the two following graphs 5.4 and 5.5. To find out if our process was done correctly, we added measurements of superluminal motion in jet of M87 from Biretta J. A., Zhou F. & Owen F. N. (1995), Biretta J. A., Sparks W. B. & Macchetto F. (1995), Meyer E. T. et al. (2013), Snios B. et al. (2019) and Kovalev Y. Y. et al. (2007).

In the parallel direction (see Figure 5.4), the jet's velocity seems to decrease with distance from AGN, which the extragalactic medium can cause. The particles from the jet are traveling. On the other hand, in the perpendicular direction (see Figure 5.5), the velocity seems to increase with the distance from AGN. This result could be explained by the reality that the particles closer to the black hole are moving more focused to the jet's center than the more distant particles.

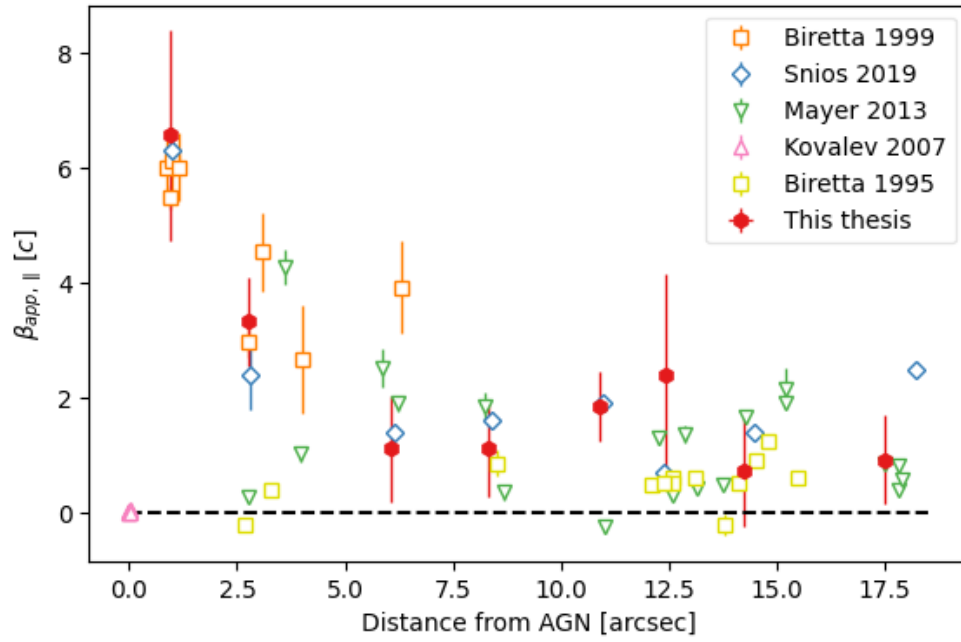


Figure 5.4: Apparent superluminal motion parallel to the jet.

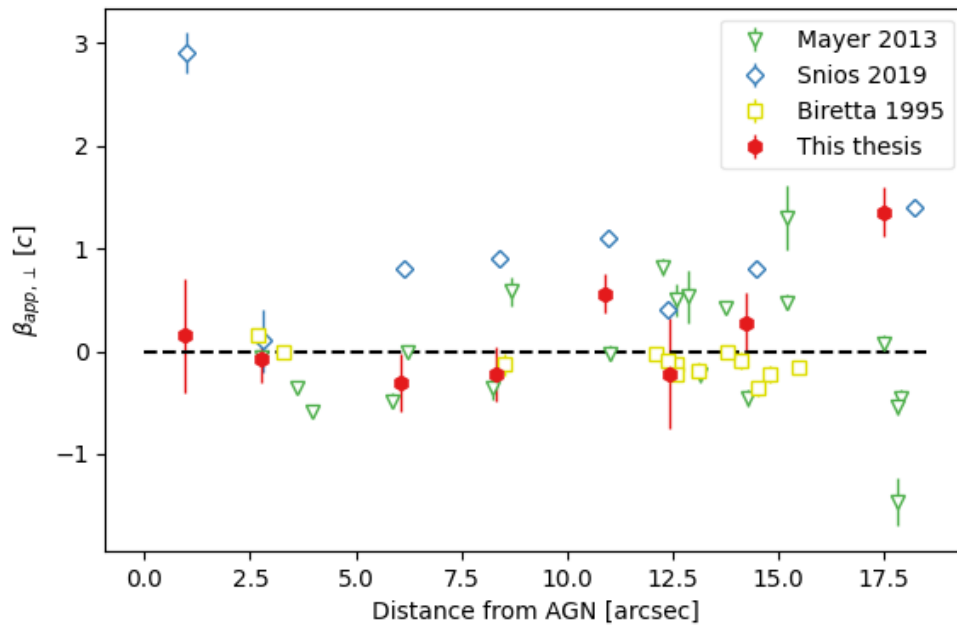


Figure 5.5: Apparent superluminal motion perpendicular to the jet.

Conclusion

In this thesis, I studied and analyzed the fine structure of the X-ray jet in the galaxy M87. The main focus was directed towards its variable morphology and movement of individual features presented in Figure 5.1 in the years 2012 and 2017. The purpose of the thesis was to get elementary knowledge of high-energy astronomy, jets structure, and to learn proper analysis of raw X-ray datasets.

In the introduction, I gave a brief overview of Active Galactic Nuclei and more deeply discussed the properties of the jet itself. The two Chandra detectors are described, including the High-Resolution camera's operational principles.

In the processing part (Section 4.1, 4.2 and 4.3), I presented the cleaning methods, and adjustments, of our raw datasets that were needed for correct analysis later on. In the remaining sections of this part (Section 4.4 and 4.5), the computational methods that have been used for precise determination of changes in brightness and position of jet's features are introduced. Due to the constructed difference map (Fig. 4.5), profound changes in brightness were expected from knots HST-1, D, E, and A. The established percentual change in brightness of knots was in agreement with our expectations from the difference map, and the maximum change was detected in knot HST-1, whose brightness increased by 64%. Variations in the brightness of the remaining knots were not so significant (see Tab. 5.1).

In the last part, I determined the parallel and perpendicular motion of individual features in the observed jet (see Tab. 5.2) and compared them to multiple scientific papers (Fig. 5.4 and 5.5). In the parallel direction, most of the knots have apparent velocity $v_{\text{app}} > c$ with the most significant $v_{\text{app}} = 6.57 \pm 1.82 c$ belonging to knot HST-1. These remarkable apparent velocities are possible to observe due to the time dilation principles from Einstein's theory of relativity combined with the small deviation angle between the jet's axis and the observer's line of sight (more information in Section 2.5). Even though it could seem like a trivial problem and solution, it was not entirely clear if we observed the move-

ment of particles or still an optical illusion. However, the results in the X-ray spectrum agree with the results in other parts of the spectrum, therefore the measured difference in the position is truly tied to the particle's movement.

Although my results are consistent within the accuracy of previous measurements, the used methods could deserve some improvements – for example, more detailed cleaning at the beginning or choosing a more complex and precise method for the astrometry correction, including the strain rate tensors, rotation tensors, and tensors of deformations.

Even though the main focus of this thesis was on learning the basic analysis of X-ray observations and getting the elementary knowledge of High Energy Astrophysics, I am still mostly fascinated by the X-ray observational technologies. Amazingly, we measured such a slight difference in position with the Chandra X-ray telescope, which has approximately ten times worse resolution than Hubble Space Telescope and a much lower count rate.

In the end, I gladly recommend this thesis as a guide for beginners or enthusiasts in X-ray astronomy who wants to get an overview of high-energy astronomy, astronomical jets or learn the basics of X-ray data processing.

Bibliography

- Aharonian F. A. (2002), ‘Proton-synchrotron radiation of large-scale jets in active galactic nuclei’, *Monthly Notices of the Royal Astronomical Society* **332**(1), 215–230.
- Biretta J. A., Sparks W. B. & Macchetto F. (1995), ‘Hubble Space Telescope observations of superluminal motion in the M87 jet’, **520**.
- Biretta J. A., Zhou F. & Owen F. N. (1995), ‘Detection of proper motions in the M87 jet’, **447**, 621.
- Blandford R. (1999), ‘Active galactic nuclei’.
- Britannica, T. E. o. E. (2019), ‘X-ray astronomy’.
URL: <https://www.britannica.com/science/X-ray-astronomy>
- Brittain, J.E. (1984), ‘Jansky discovers extraterrestrial radio noise.’, *IEEE Proceedings* **72**(6), 709–714.
- Caballero J. A. , Albacete-Colombo J. F. & López-Santiago J. (2010), ‘HRC-I/Chandra X-ray observations towards σ Orionis’, *Astronomy and astrophysics* **521**, A45.
- Castelvecchi D. (2019), ‘Black hole pictured for first time — in spectacular detail’, *Nature* **568**(7752), 284–285.
- Center for Astrophysics (2021), ‘SAOImageDS9’.
URL: <https://sites.google.com/cfa.harvard.edu/saoimageds9>
- Chandra X-ray Center (2020), ‘Acis: Advanced ccd imaging spectrometer’.
URL: <https://cxc.harvard.edu/proposer/POG/html/chap6.html>
- Chandra X-ray observatory (2008), ‘Chandra specifications’.
URL: <https://chandra.harvard.edu/about/specs.html>

- Davelaar J. , Olivares H. , Porth O. , Bronywaer T. , Janssen M., Roelofs F. and Mizuno Y. , Fromm C. M. , Falcke H. & Rezzolla L. (2019), ‘Modeling non-thermal emission from the jet-launching region of M 87 with adaptive mesh refinement’, *Astronomy and Astrophysics* **632**, A2.
- EHT Collaboration (2019), ‘First image of a black hole gets a polarizing update that sheds light on magnetic fields’.
URL: <https://www.space.com/first-black-hole-image-polarized-m87>
- Fleishman G. D. (2006), ‘Diffusive synchrotron radiation from extragalactic jets’, *Monthly Notices of the Royal Astronomical Society: Letters* **365**(1), L11–L15.
- Four Peaks Technologies (2012), ‘Black hole active galaxies’.
URL: <http://www.blackholecentral.com/index.html>
- Graham A. W. & Soria R. (2019), ‘Expected intermediate-mass black holes in the Virgo cluster - I. Early-type galaxies’, *Monthly Notices of the Royal Astronomical Society* **484**(1), 794–813.
- Harvard-Smithsonian Center for Astrophysics (2014), ‘Chandra fun facts’.
URL: <https://chandra.harvard.edu/about/fun/index.html>
- Howell Elizabeth (2018), ‘Chandra space telescope: Revealing the invisible univers’.
URL: <https://www.space.com/18669-chandra-x-ray-observatory.html>
- HS Center for Astrophysics (2019), ‘Science instruments’.
URL: <https://chandra.harvard.edu/about/science.instruments.html>
- Iafrate G. & Ramella M. (2015), *The Messier Catalog*.
- Kovalev Y. Y. , Lister M. L. , Homan D. C. & Kellermann K. I. (2007), ‘The Inner Jet of the Radio Galaxy M87’, **668**.
- Meyer E. T., Eileen T. , Sparks W. B. , Biretta J.A. , Anderson J. and Sohn S. T. & van der Marel R. P. and Norman C. and Nakamura M. (2013), ‘Optical Proper Motion Measurements of the M87 Jet: New Results from the Hubble Space Telescope’, *The Astrophysical Journal Letters* **774**(2), L21.
- MSFC Chandra IPI Teams (2020), ‘Hrc: High resolution camera’.
URL: <https://cxc.harvard.edu/proposer/POG/html/chap7.html>

- Nakamura M. , Garofalo D. & Meier D. L. (2010), ‘A Magnetohydrodynamic Model of the M87 Jet. I. Superluminal Knot Ejections from HST-1 as Trails of Quad Relativistic MHD Shocks’, *The Astrophysical Journal* **721**(2), 1783–1789.
- National Science Foundation (1999), ‘Close-up look at a jet near a black hole in galaxy m87’.
URL: <https://esahubble.org/images/opo9943b/>
- Nimiroff R. & Bonnell J. (2001), ‘M87’s energetic jet’.
URL: <https://apod.nasa.gov/apod/ap011101.html>
- Perlman E. S. , Biretta J. A. , Zhou F. & Sparks W. B. (1999), ‘Optical and radio polarimetry of the m87 jet at 02 resolution’, *The Astronomical Journal* .
- Rees M. J. (1966), ‘Appearance of Relativistically Expanding Radio Sources’, *Nature* **211**(5048), 468–470.
- Rosswog S. & Brüggen M. (2011), *Introduction to High-Energy Astrophysics*.
- Safarzadeh M. , Loeb A. & Reid M. (2019), ‘Constraining a black hole companion for M87* through imaging by the Event Horizon Telescope’, *Monthly Notices of the Royal Astronomical Society: Letters* **488**(1), L90–L93.
URL: <http://dx.doi.org/10.1093/mnrasl/slz108>
- Sauty C., Tsinganoi K. & Trussoni E. (2001), ‘Jet formation and collimation in agn and μ -quasars’, *arXiv preprint astro-ph/0108509* .
- Semenov V. , Dyadechkin S. & Punsly B. (2004), ‘Simulations of Jets Driven by Black Hole Rotation’, *Science* **305**(5686), 978–980.
- Singal A. K. (2016), ‘Relativistic doppler beaming and misalignments in agn jets’, *The Astrophysical Journal* **827**(1), 66.
URL: <http://dx.doi.org/10.3847/0004-637X/827/1/66>
- Smithsonian Astrophysical Observatory (2021), ‘Chandra at a glance’.
URL: <https://cxc.harvard.edu/cdo/about.chandra/>
- Smithsonian Institution (2013a), ‘Correcting Absolute Astrometry’.
URL: <https://cxc.cfa.harvard.edu/ciao/threads/reproject.aspect/>

- Smithsonian Institution (2013*b*), ‘Dmcopy’.
URL: <https://cxc.cfa.harvard.edu/ciao/ahelp/dmcopy.html>
- Smithsonian Institution (2013*c*), ‘Fluximage’.
URL: <https://cxc.harvard.edu/ciao/ahelp/dmstat.html>
- Smithsonian Institution (2019), ‘Filtering Lightcurve’.
URL: <https://cxc.cfa.harvard.edu/ciao/threads/filter.ltcrv/>
- Smithsonian Institution (2020*a*), ‘Chandra repro’.
URL: <https://cxc.cfa.harvard.edu/ciao/ahelp/chandra.repro.html>
- Smithsonian Institution (2020*b*), ‘Dmimgcalc’.
URL: <https://cxc.cfa.harvard.edu/ciao/ahelp/dmimgcalc.html>
- Smithsonian Institution (2021), ‘Fluximage’.
URL: <https://cxc.cfa.harvard.edu/ciao/ahelp/fluximage.html>
- Smithsonian Institution (2021), ‘Observation Interactive Analysis of Observations’.
URL: <https://cxc.cfa.harvard.edu/ciao/>
- Snios B. , Nulsen E. J. , Kraft R. P. and Cheung C. C. , Meyer E. T. and Forman W. R. , Jones Ch. & Murray S. S. (2019), ‘Detection of Superluminal Motion in the X-Ray Jet of M87’, *The Astrophysical Journal* **879**(1), 8.
- Sokol Joshua (2017), ‘Trick of the light’.
URL: <https://www.newscientist.com/article/2131889-weird-energy-beam-seems-to-travel-five-times-the-speed-of-light/>
- Swinburne University of Technology (n.d.), ‘The sao encyclopedia of astronomy’.
URL: <https://astronomy.swin.edu.au/cosmos/J/Jets>
- Thorne Kip (1994), *Black Holes and Time Warps*.
- Walker R. C. , Davies F. B. , Hardee P. E. , Ly C. & Junor W. (2018), ‘The structure and dynamics of the subparsec jet in m87 based on 50 VLBA observations over 17 years at 43 GHz’, *The Astrophysical Journal* **855**(2), 128.
URL: <https://doi.org/10.3847/1538-4357/aaafcc>
- X-Ray center (2021), ‘Observation search’.
URL: <https://cda.harvard.edu/chaser/>